Strain-induced lead-free morphotropic phase boundary

Reza Ghanbari[1], Harikrishnan KP[2], Kinnary Patel[3], Hua Zhou[4], Tao Zhou[5], Rui Liu[5], Liyan Wu[6], Aarushi Khandelwal[7, 8], Kevin J. Crust[8, 9], Sankalpa Hazra[10], John Carroll[11, 12], Cedric J. G. Meyers[6], Jiayue Wang[7, 8], Sergey Prosandeev[3], Huimin Qiao[1], Young-Hoon Kim[13], Yoji Nabei[14], Miaofang Chi[13, 15], Dali Sun[13], Nina Balke[1], Martin Holt[5], Venkatraman Gopalan[10], Jonathan E. Spanier[6,11,16], David A. Muller[2,17], Laurent Bellaiche[3,18], Harold Y. Hwang[7, 8], Ruijuan Xu[1*]

[1] Department of Materials Science and Engineering, North Carolina State University, Raleigh, NC, USA
[2] School of Applied and Engineering Physics, Cornell University, Ithaca, NY, USA
[3] Smart Ferroic Materials Center, Physics Department and Institute for nanoscience and Engineering, University of Arkansas, Fayetteville, Arkansas, USA
[4] X-ray Science Division, Advanced Photon Source, Argonne National Laboratory, Lemont, IL, USA
[5] Center for Nanoscale Materials, Argonne National Laboratory, Lemont, IL, USA
[6] Department of Mechanical Engineering and Mechanics, Drexel University, Philadelphia PA, USA
[7] Department of Applied Physics, Stanford University, Stanford, CA, USA
[8] Stanford Institute for Materials and Energy Sciences, SLAC National Accelerator Laboratory, Menlo Park, CA, USA
[9] Department of Physics, Stanford University, Stanford, CA, USA
[10] Department of Materials Science and Engineering, The Pennsylvania State University, University Park, PA, USA
[11] Department of Electrical and Computer Engineering, Drexel University, Philadelphia, PA, USA
[12] DEVCOM C5ISR U.S. Army, Aberdeen Proving Grounds, MD, USA
[13] Center for Nanophase Materials Sciences (CNMS), Physical Sciences Directorate (PSD) Oak Ridge National Laboratory, Oak Ridge, TN, USA
[14] Department of Physics, North Carolina State University, Raleigh, NC, USA
[15] Thomas Lord Department of Mechanical Engineering and Materials Science, Durham, NC, USA
[16] Departments of Materials Science and Engineering, Drexel University, Philadelphia, PA, USA
[17] Kavli Institute at Cornell for Nanoscale Science, Ithaca, NY, USA
[18] Department of Materials Science and Engineering, Tel Aviv University, Ramat Aviv, Tel Aviv 6997801, Israel.

*Email: rxu22@ncsu.edu

Abstract

Enhanced susceptibilities in ferroelectrics often arise near phase boundaries between competing ground states. While chemically-induced phase boundaries have enabled ultrahigh electrical and electromechanical responses in lead-based ferroelectrics, precise chemical tuning in lead-free alternatives, such as (K,Na)NbO_3 thin films, remains challenging due to the high volatility of alkali metals. Here, we demonstrate strain-induced morphotropic phase boundary-like polymorphic nanodomain structures in chemically simple, lead-free, epitaxial $NaNbO_3$ thin films. Combining *ab initio* simulations, thin-film epitaxy, scanning probe microscopy, synchrotron X-ray diffraction, and electron ptychography, we reveal a labyrinthine structure comprising coexisting monoclinic and bridging triclinic phases near a strain-induced phase boundary. The coexistence of energetically competing phases facilitates field-driven polarization rotation and phase transitions, giving rise to a multi-state polarization switching pathway and large enhancements in dielectric susceptibility and tunability across a broad frequency range. Our results open new possibilities for engineering lead-free thin films with enhanced functionalities for next-generation applications.

Introduction

Ferroelectric materials often exhibit ultrahigh electrical and electromechanical responses near phase boundaries where competing ground states coexist. A notable example is the morphotropic phase boundary (MPB) in lead zirconium titanate ($PbZr_{1-x}Ti_xO_3$, PZT), a transition region in the composition-temperature phase diagram marked by an abrupt change in crystal symmetry[1–6]. The flattening of the free energy profile at the MPB facilitates polarization rotation among different phases under external fields, leading to remarkable dielectric and piezoelectric performance[2,7,8]. However, despite these advantages, the presence of toxic lead in PZT raises

significant environmental and health concerns, particularly for implantable bio-micro-electromechanical systems (bio-MEMS) and *in vivo* piezoelectric sensors[9,10]. Thus, there is an urgent need for lead-free alternatives with comparable or superior performance.

Among lead-free ferroelectrics, potassium sodium niobate ($(K,Na)NbO_3$, KNN) has emerged as a promising candidate, attracting substantial research interest over the past two decades[11,12]. Most research efforts have focused on enhancing susceptibilities in KNN-based bulk ceramics by constructing multi-phase boundaries through chemical substitutions[13–19]. However, with the increasing demand for device miniaturization, developing lead-free thin films with ultrahigh electrical and mechanical susceptibilities is crucial for applications such as micro- and nano-electromechanical systems (MEMS and NEMS)[20]. Chemically-driven phase boundaries, however, often introduce compositional complexity, leading to structural disorder and heterogeneity that degrade thin-film crystallinity[21,22]. Moreover, the high volatility of alkali metals makes precise chemical tuning of KNN-based thin films particularly challenging. To overcome these limitations, alternative approaches beyond chemical methods are essential for constructing phase boundaries in lead-free ferroelectric thin films.

Epitaxial strain, arising from lattice mismatch between thin films and substrates, offers a promising alternative approach for creating MPB-like phase boundaries in lead-free ferroelectrics. For instance, under compressive strain larger than -4%, $BiFeO_3$ undergoes a phase transition to a highly distorted tetragonal-like phase, forming a mixed-phase structure comprising tetragonal-like and rhombohedral-like phases, which results in ultrahigh electromechanical responses[23–28]. Additionally, recent studies have demonstrated improved dielectric and piezoelectric properties in epitaxially $BaTiO_3$ films, arising from a strain-induced bridging phase[29] and a slush-like polar structure composed of coexisting phases with varying symmetries[30]. Despite the promise of strain-

engineered phase boundaries, this approach remains underexplored in KNN based thin films. To explore strain-induced MPB-like structures in these materials, we focus on sodium niobate ($NaNbO_3$), a key end-member of the KNN family, known for its rich structural polymorphism and numerous phase transitions. The small energy barriers between nearly degenerate phases in $NaNbO_3$ allow for structural modulation through a small thermal, electrical, or mechanical perturbations, providing possibility for enabling multi-phase boundaries with enhanced functionalities[31]. While $NaNbO_3$ bulk ceramics have been extensively studied for decades as promising lead-free electroceramics for energy storage applications[32–36], research on $NaNbO_3$ thin films remains in its early stages but is rapidly gaining attention[37–44]. Recent advances in thin-film synthesis have enabled the growth of high-quality $NaNbO_3$ films, unlocking their potential for ultrahigh electromechanical responses[45,46]. Furthermore, electron ptychography has recently revealed an unconventional microscopic picture in $NaNbO_3$ films, where ferroelectricity is dominated by the anion displacements relative to the niobium sublattice[47].

Here, combining epitaxial *ab initio* simulations, epitaxial thin-film synthesis, electrical measurements, and detailed structural characterizations via scanning probe microscopy, synchrotron X-ray diffraction, and electron ptychography, we design and construct strain-induced MPB-like polymorphic structures with enhanced dielectric and ferroelectric properties in $NaNbO_3$ heterostructures. Our strategy is to leverage a slight strain perturbation from the substrate to manipulate structural instabilities among nearly degenerate phases in $NaNbO_3$ thin films, thereby inducing a multi-phase boundary. The coexisting polymorphs near the phase boundary facilitate continuous polarization rotation, resulting in a multi-state switching pathway and large enhancements in dielectric susceptibility and tunability across a broad frequency range.

Results and Discussion

Design and synthesis of strain-induced multi-phase boundary in $NaNbO_3$ films

Bulk $NaNbO_3$ exhibits a complex phase diagram with multiple temperature-dependent phase transitions. At room temperature, it typically adopts an orthorhombic antiferroelectric *Pbcm* phase, which can be irreversibly switched into a ferroelectric $Pmc2_1$ phase under an electrical field. Our density functional theory (DFT) simulations (Fig. 1a) further reveal additional competing ferroelectric polymorphs in $NaNbO_3$ thin films that are energetically favorable near the bulk lattice of $NaNbO_3$ ($a \sim 3.88 - 3.915$ Å). This suggests the possibility of phase transitions or polymorph coexistence in $NaNbO_3$ thin films under small strain. These polymorphs include phases with space group symmetries *Cm*, *Pc*, and *Cc*, each exhibiting distinct polarization configurations and oxygen octahedral tilts (Fig. 1b and Supplementary Fig. 1). Given the intricate energy balance among these competing phases, we aim to experimentally realize MPB-like structures with coexisting ferroelectric polymorphs in $NaNbO_3$ heterostructures to enable giant enhancements in dielectric and ferroelectric properties via strain engineering.

To induce varying strain states in the thickness series via strain relaxation, we synthesize epitaxial $NaNbO_3$ films with thicknesses ranging from 25 to 185 nm on (001)-oriented single crystalline $SrTiO_3$ substrates, with atomically smooth interfaces (Supplementary Fig. 2) using pulsed laser deposition (PLD). X-ray reflectivity (XRR) is employed to calibrate the thickness of 25 nm films and determine the growth rate for thicker films (Supplementary Fig. 3a). The thickness-dependent structural evolution of the $NaNbO_3$ films is further examined through high-resolution X-ray θ - 2θ scans (Fig. 1c and Supplementary Fig. 3b, c). The presence of Laue fringes indicates the high crystalline quality of the films. Notably, films with a thickness $t \geq 80$ nm exhibit a broadened peak near the $NaNbO_3$-002 diffraction condition, suggesting the presence of multiple

diffraction peaks in $NaNbO_3$ films, potentially associated with either distinct structural phases or different structural domain variants (Fig. 1c). To further explore this structural evolution, we study the film topography using atomic force microscopy (AFM). While 25 nm films exhibit atomically smooth surfaces, intriguing labyrinthine topography emerge in films with $t \geq 80$ nm (Figs. 1d-g). These patterns, consisting of stripe-like features oriented along the pseudocubic [100] and [010], exhibit increasing ordering as thickness increases. The labyrinthine structures introduce regions of elevated "walls" and lowered "pathways" in the film topography, which possibly contributes to the broadening of diffraction peaks observed in θ - 2θ scans. These labyrinthine patterns may arise from the coexistence of either structural phases with varying symmetries or domain variants with the same symmetry.

Ferroelectric domain structure characterization

To further elucidate the structural nature of the labyrinthine pattern, we examine the ferroelectric domain structures of $NaNbO_3$ films using piezoresponse force microscopy (PFM) (Supplementary Fig. 4). PFM imaging reveals that the "walls" and the "pathways" of the labyrinthine pattern correspond to two distinct sets of ferroelectric polydomain structures, both exhibiting ultra-fine nanoscale domains and a high density of domain walls. These polydomain regions exhibit different PFM amplitude responses: the "walls" show a stronger vertical response than the "pathways", indicating a larger out-of-plane polarization component (Fig. 2a, c, e), while the "pathways" display a stronger lateral response, suggesting a larger in-plane polarization component (Fig. 2b, d, f). Detailed analysis of vertical and lateral PFM amplitude and phase signals, performed by varying the relative orientation between the PFM cantilever and sample (Supplementary Fig. 5), suggests that the "pathways" exhibit an in-plane polarization component

along the pseudocubic [110] or [1-10] (Fig. 2g), whereas the "walls" possess an in-plane polarization component along the pseudocubic [100] or [010] (Fig. 2h). Combining both the in-plane and out-of-plane signals as well as the projected domain wall orientation, we propose the following polarization configurations: the "pathways" adopt a polydomain structure with polarizations along [*xxz*] or [*x*-*xz*] (where $x > z$, given the stronger in-plane response; Fig. 2g), and the "walls" possess polarizations along [*x*0*z*] or [0*xz*] (where $x < z$, given the stronger out-of-plane response; Fig. 2h). Following established nomenclature used for similar polarization configurations in MPB PZT[49], we designate these phases as "M_C" and "M_B", respectively. Each phase allows four possible polarization variants (eight if considering out-of-plane inversion), forming various polydomain configurations with (010)- or (100)-type domain walls. Here we provide illustrations for charge-neutral configurations with oppositely aligned out-of-plane polarization in adjacent domains (Fig. 2g, h), Additionally, we also probe the potential presence of polydomain structures with charged domains walls in the films, where adjacent domains exhibit identical out-of-plane polarization direction. Based on PFM vertical amplitude contrast, we further analyze the areal fraction evolution of these phases as a function of thickness. The M_B phase increases from 14% in 25 nm films to 73% in 185 nm films, with the M_C phase following the opposite trend (Fig. 2i). These observations suggest that thinner films favor the M_B phase with a larger out-of-plane polarization, whereas thicker films favor the M_C phase with a larger in-plane polarization. This phenomenon is likely driven by the thickness-dependent strain evolution in $NaNbO_3$ films: the compressive strain in thinner films stabilizes a phase with enhanced out-of-plane distortion, whereas strain relaxation in thicker films stabilizes a phase with increased in-plane distortion.

Characterizing mixed-phase via synchrotron X-ray diffraction and electron ptychography

Given the nanoscale domain sizes approaching the resolution limit of PFM, we perform additional structural characterizations to further verify these phases and uncover additional structural details. First, we conduct second harmonic generation (SHG) polarimetry measurements to characterize the symmetry of the coexisting phases. Electric dipole SHG is a nonlinear optical process where incident light at a fundamental frequency, ω, is converted into second harmonic light at frequency, 2ω, by the interacting material owing to its broken inversion symmetry (Supplementary Fig. 6a). SHG polar plots are measured by rotating the polarization of the incident fundamental light while measuring the reflected SHG intensities corresponding to both polarization directions (*p*- and *s*-polarized) for each film thickness (Supplementary Fig. 6b-d). Following PFM observations, the polar plots are fitted using a multi-domain model assuming the coexistence of M_C and M_B phases, each consisting of four domain variants. It is important to note that, while our measurements are well fitted by this monoclinic multi-domain model, other structural models like multi-domain orthorhombic or rhombohedral models can also be used to fit the polar plots.

To further confirm the monoclinic distortion, we conduct X-ray reciprocal space mapping (RSM) to resolve the structural details of the coexisting phases. RSM has been applied in previous studies as a powerful method for identifying and differentiating monoclinic symmetries in oxide ferroelectrics[50–52]. We conduct RSMs around the $NaNbO_3$-002 diffraction condition using both lab-source and synchrotron-based XRD (Fig. 3a and Supplementary Figs. 7a and 8). Diffraction peaks corresponding to $NaNbO_3$ appear at higher and lower Q_y positions with respect to $SrTiO_3$-002. Based on peak positions, the calculated *c*-lattice parameters are ~ 3.891 Å and ~ 3.944 Å, corresponding to the M_B and M_C phases with lower and higher topographic heights, respectively.

The intensity of these peaks evolves with thickness, with M_C being more pronounced in 25 nm films and M_B dominating at greater thickness, consistent with the trend observed in PFM imaging (Supplementary Fig. 7a). Based on the shift of the 002-diffraction peak, we quantify the thickness-dependent evolution of out-of-plane strain for each phase and estimate the average out-of-plane strain in the mixed-phase state by weighting the strain of each phase according to its areal fraction, as extracted from PFM imaging (Supplementary Fig. 7b, c). The corresponding in-plane compressive strain is estimated by converting the out-of-plane strain using the Poisson effect under biaxial strain conditions (Supplementary Fig. 7d). These results reveal a gradual decrease in both out-of-plane tensile strain and in-plane compressive strain with increasing film thickness, consistent with strain relaxation. To further investigate potential compositional effects, we perform X-ray photoelectron spectroscopy (XPS) on $NaNbO_3$ films with varying thicknesses. While the XPS results show that the films are sodium deficient, there is no significant variation in Na/Nb ratio across the thickness series (Supplementary Fig. 9), indicating that the structural evolution is not driven by changes in sodium stoichiometry. Instead, it is governed directly by strain evolution: in thinner films, compressive strain stabilizes the M_C-dominated mixed-phase state with a larger *c*-lattice parameter, whereas strain relaxation in thicker films reduces the *c*-axis distortion, favoring the M_B-dominated mixed-phase state.

Further insights into monoclinic distortion were obtained from the $NaNbO_3$-103 diffraction condition. The 103-diffraction peak splits into two adjacent peaks for the M_B phase (Fig. 3d) and three adjacent peaks for the M_C phase (Fig. 3e and Supplementary Fig. 10), indicative of four-domain configuration in each phase[45,51]. These characteristic peak splitting confirms the presence of monoclinic distortion of the coexisting phases. Beyond these monoclinic features, we also observe four-fold symmetric satellite peaks surrounding the M_B and M_C in 002-diffraction,

exhibiting similar L but opposite H values (Fig. 3b, c). The first set, with L ~ 2.013, corresponds to a triclinic phase (Tri-1, Fig. 3a, b) with a c-lattice parameter of ~3.885 Å and a tilt angle of 0.43° along [100] relative to the substrate normal. Similarly, another set, with L ~ 1.995, corresponds to a second triclinic phase (Tri-2, Fig. 3a, c) with a c-lattice parameter of ~3.951 Å and a tilt angle of 0.29° along [100]. These triclinic phases, previously also observed in other mixed-phase systems[52], act as bridging phases between M_B and M_C (Fig. 3g). To directly visualize the real-space distribution of monoclinic and triclinic phases, we perform scanning diffraction X-ray microscopy (SDXM). This technique employs a focused, coherent synchrotron X-ray beam to scan point by point across the sample, enabling phase mapping by selecting specific diffraction peaks including those satellite peaks. Using this approach, we map the distributions of M_B, M_C, and Tri-1 phases (Fig. 3f), where the triclinic phases appear near the M_B–M_C boundary region. These observations further corroborate the bridging phase nature for these triclinic phases, with the polarization rotating between the M_B and M_C phases (Fig. 3g).

To further elucidate the spatial distribution of the coexisting phases across the film thickness, we perform scanning transmission electron microscopy (STEM) studies on mixed-phase $NaNbO_3$ (Fig. 3h). We observe the segmentation of two phases (Fig. 3i and Supplementary Fig. 11), differentiated by the presence (Fig. 3j) and absence (Fig. 3k) of half-order satellite spots in the diffraction patterns, corresponding to in-phase and anti-phase oxygen octahedra tilts, respectively. Electron ptychography further resolves these tilt modes in real space, where in-phase and anti-phase tilts manifest as single (Fig. 3l and Supplementary Fig. 12a) and double (Fig. 3m and Supplementary Fig. 12b) oxygen columns in projection, respectively. Combining these findings with DFT simulations (Supplementary Fig. 1), we identify the in-phase tilted structures as *Pc* ($a^+b^+c^-$) or *Cm* ($a^+b^+c^+$) and the anti-phase tilted structure as *Cc* ($a^-a^-c^-$). The simulated

polarization profiles for *Pc*/*Cm* and *Cc* are also consistent with the polarization configurations for the M_C and M_B phases analyzed from PFM characterizations. These results further confirm the coexistence of monoclinic *Pc*/*Cm* (M_C) and *Cc* (M_B) phases in the mixed-phase $NaNbO_3$ films.

Multi-state polarization switching

To understand how mixed-phase states influence macroscale properties, we conduct electrical measurements to examine the ferroelectric switching behavior of $NaNbO_3$ films using a vertical capacitor geometry with symmetric $La_{0.7}Sr_{0.3}MnO_3$ electrodes (Methods). Well-defined, fully saturated polarization-electric field (P-E) hysteresis loops were measured over a broad frequency range from 1 Hz to 10 kHz, exhibiting low leakage in the synthesized films (Fig. 4a and Supplementary Fig. 13). Both the saturated and remanent polarizations are significantly enhanced compared to previous studies on $NaNbO_3$[44,45,53–56], due to the presence of M_C phase with enhanced out-of-plane polarization. Maximum values of 53 $\mu C/cm^2$ in saturated polarization and 40 $\mu C/cm^2$ in remanent polarization were observed in 80 nm films. To further investigate the switching kinetics, we employ the positive-up negative-down (PUND) method, probing switched remanent polarization as a function of pulse voltage at varying pulse widths (Fig. 4b and Supplementary Fig. 14). Notably, the films exhibit multi-state polarization switching, with the intermediate-state polarization increasing from 28.05 $\mu C/cm^2$ in 80 nm films to 54.10 $\mu C/cm^2$ in 185 nm films (Fig. 4b). To elucidate the structural mechanism underlying this multi-state switching behavior, we perform local-scale PFM imaging by applying a DC bias within a defined region of the $NaNbO_3$ films. By characterizing the evolution of film topography under increasing applied bias, we identify the following switching pathway: Initially, at a pre-poled bias of -6V, the film exhibits a uniform elevated topography (Fig. 4c). Upon applying a positive bias, a labyrinthine pattern

emerges, exhibiting elevated "walls" and lowered "pathways", indicative of mixed-phase formation (Fig. 4d). Further increasing the bias transforms the labyrinthine pattern back into a uniform elevated topography (Fig. 4e). These observations suggest a field-driven phase evolution in $NaNbO_3$ films. Initially, the films are uniformly switched into the negatively poled M_C phase. Upon applying a positive bias, the M_C phase first transitions into an intermediate state, consisting of coexisting negatively poled M_C and positively poled M_B phases, before fully switching into a positively poled Mc phase at higher bias (Fig. 4f). The polarization evolution of these intermediate states aligns with the net polarization calculated for the mixed phase at each film thickness (Supplementary Table 1). These results confirm that the observed multi-state switching in mixed-phase $NaNbO_3$ originates from phase transitions between monoclinic phases in $NaNbO_3$. Moreover, we evaluate the endurance of stability of both the fully switched and intermediate polarization states. Our results demonstrate that the films exhibit minimal fatigue after more than 10^8 writing cycles, with less than a 10% change in remanent polarization (Supplementary Fig. 15a, b). Retention tests further confirm the long-term stability of both the fully switched and intermediate polarization states (Supplementary Fig. 15c). These results highlight the robustness of the multi-state switching behavior and demonstrate the potential of mixed-phase $NaNbO_3$ films for reliable non-volatile multi-state memory and logic applications.

Enhanced dielectric susceptibility and tunability

With the presence of mixed phases and multi-state switching in $NaNbO_3$, how do these structural features influence the dielectric properties? Could they enhance susceptibility similarly to MPB PZT films? To explore this, we further investigate the dielectric properties of mixed-phase $NaNbO_3$ films. First, we perform Rayleigh analysis by measuring dielectric permittivity under

increasing AC excitation fields (Supplementary Fig. 16a). Using the Rayleigh law ($\varepsilon' = \varepsilon'_{init} + \alpha' E_0$)[57], we extract the reversible Rayleigh coefficient (ε'_{init}) in the linear regime, which accounts for contributions from intrinsic lattice and reversible domain wall motion, as well as the irreversible Rayleigh coefficient (α') in the nonlinear regime, which describes the extrinsic contribution from irreversible domain wall motion. Notably, the Rayleigh coefficients peak in 80 nm films, consistent with the thickness-dependent domain wall density observed in PFM imaging (Supplementary Fig. 16b and 17). These results indicate that the extrinsic contribution from both reversible and irreversible domain wall motion to dielectric permittivity correlates with domain wall line density in $NaNbO_3$ films. The high density of domain walls in mixed-phase $NaNbO_3$ leads to a significant enhancement in extrinsic domain wall contributions, resulting in increased domain wall mobility.

To further investigate the dielectric performance in the linear regime, we measured dielectric permittivity and loss tangent under low AC excitation fields across a frequency range of 20 Hz to 10 kHz (Fig. 5a). The results reveal an ultra-low loss tangent increasing with frequency, ranging from 0.021 to 0.067 in 185 nm films. Meanwhile, the measured permittivity exhibits a slight decrease with frequency, with a peak value of 977 observed in 80 nm films at 20 Hz. Among the examined thicknesses, the 80 nm films exhibit the highest permittivity, followed by 25 nm, 125 nm, and 185 nm films, consistent with the trend in domain wall density. Notably, even the 185 nm films show a high permittivity of up to 637. This enhancement arises from both intrinsic and extrinsic mechanisms. Intrinsically, the coexistence of monoclinic and triclinic phases facilitates continuous rotation of polarization under an applied electric field, thereby increasing dielectric susceptibility. Extrinsically, the high density of domain walls enhances reversible domain wall motion, which further contributes to enhanced susceptibility. Notably, this enhancement is

comparable to, or even exceeds, previously reported values for MPB PZT films[58–61] (600 - 1300 depending on film thickness, processing, and crystallographic orientation in polycrystalline films).

Finally, we demonstrate how the mixed-phase structure enables exotic and highly tunable dielectric properties, which are critical for electronically tunable filters, antennas, resonators, and phase shifters in wireless communication systems. Upon applying a DC electric field, we observe enhanced tunability at room temperature across a broad frequency range, from 1 kHz to microwave frequencies (5 GHz - 18 GHz). At low frequencies and under DC fields below the coercive field, we measure a hysteresis-free tunability ranging from 45% to 82%, with a peak value of 82% in 80 nm films (Fig. 5b). When increasing the DC field beyond the coercive field, tunability is further enhanced, ranging from 75% to 92%, again peaking at 92% in 80 nm films while maintaining a low loss tangent (Fig. 5c). Intriguingly, unlike conventional negative tunability, where permittivity continuously decreases with increasing DC field, mixed-phase $NaNbO_3$ exhibits an unconventional tunability response with a plateau in dielectric permittivity at low fields, remaining stable until a higher field induces further dielectric suppression (Fig. 5c). This unconventional behavior is attributed to the multi-state switching pathway in mixed-phase $NaNbO_3$, where an intermediate mixed phase state (i.e., coexistence of negatively poled M_B and positively poled M_C or *vice versa*) maintains minimal permittivity change under a DC field. This unconventional tunability extends into microwave frequencies. Using an interdigital capacitor geometry, we observe tunability ranging from 26% to 54% across 5–18 GHz, while maintaining a low loss tangent (Fig. 5d and Supplementary Fig. 18). The relatively lower capacitance modulation in this in-plane geometry, compared to the vertical capacitor geometry used for low-frequency measurements, is attributed to the underlying $SrTiO_3$ substrate, which contributes significantly to the total capacitance but remains non-tunable under applied fields (Methods). Despite this

substrate effect, the mixed-phase $NaNbO_3$ still exhibits highly tunable dielectric properties at microwave frequencies. Future work will explore alternative device architectures designed to mitigate substrate effects and further elucidate the high-frequency tunability mechanisms in mixed-phase $NaNbO_3$.

Outlook

Our work highlights a strain-induced phase boundary in chemically simple, lead-free ferroelectric thin films. We demonstrate strain-induced MPB-like polymorphic nanodomain structures composed of coexisting monoclinic and bridging phases, which drive significant enhancements in dielectric susceptibility and tunability. These enhancements are comparable to or even surpass those of PZT films near MPB compositions, arising from both continuous polarization rotation among the coexisting polymorphs and extrinsic contributions due to the motion of a high density of domain walls. Additionally, we uncover field-driven transitions between monoclinic phases that enable multi-state polarization switching and unconventional tunability behavior across a broad frequency range. Notably, $NaNbO_3$ exhibits a unique ability to undergo allotropic modifications at a much lower strain level than other lead-free perovskite oxides such as $BiFeO_3$, due to its structural richness. This advantage allows the use of a broader range of commercially accessible substrates that provide modest strain to induce and tune the phase boundary. Beyond the MPB-like boundary, the structural complexity of $NaNbO_3$ also allows for the creation of various multi-phase boundaries involving different crystal symmetries and ferroic orders via strain engineering. Moreover, mixed-phase $NaNbO_3$ exhibits significantly lower leakage currents compared to mixed-phase $BiFeO_3$, enabling direct measurement of its intrinsic ferroelectric and dielectric properties near the strain-induced phase boundary. However, the

underlying leakage mechanism requires further investigation in future studies. Additionally, the ultrahigh low-frequency tunability (up to 92%) observed in mixed-phase $NaNbO_3$ suggests the promise of enhanced microwave tunability using alternative device architectures that minimize substrate effects. This positions $NaNbO_3$ as a potential alternative to conventional tunable dielectrics such as $(Ba,Sr)TiO_3$ (BST). More broadly, our findings open new opportunities for strain-engineered mixed-phase states in other lead-free perovskites, particularly in underexplored KNN-based thin films, for next-generation dielectric and ferroelectric applications.

Methods

Thin-film synthesis

Epitaxial heterostructures consisting of $NaNbO_3$ films and $La_{0.7}Sr_{0.3}MnO_3$ electrode layers were synthesized on (001)-oriented single-crystalline $SrTiO_3$ substrates via pulsed laser deposition. The synthesis of 10 nm thick $La_{0.7}Sr_{0.3}MnO_3$ bottom electrode layer was conducted in a dynamic oxygen pressure of 190 mTorr, at a growth temperature of 730 °C, a laser fluence of 1.6 J /cm^{-2}, and a repetition rate of 3 Hz, using a 3.7 mm² imaged laser spot. The synthesis of $NaNbO_3$ films with thicknesses ranging from 25 nm to 185 nm was conducted in a dynamic oxygen pressure of 210 mTorr, at a growth temperature of 660 °C, a laser fluence of 2.1 J cm^{-2}, and a repetition rate of 2 Hz, using a 4.58 mm^2 imaged laser spot. For fabricating $NaNbO_3$ capacitor structures, a 60 nm thick $La_{0.7}Sr_{0.3}MnO_3$ top electrode layer was synthesized right after the growth of $NaNbO_3$ to form a tri-layer heterostructure. The synthesis of the top electrode layer was conducted in a dynamic oxygen pressure of 190 mTorr, at a growth temperature of 660 °C, a laser fluence of 1.6 J cm^{-2}, and a repetition rate of 3 Hz, using a 3.7 mm^2 imaged laser spot. Following synthesis, all samples were cooled down to room temperature at a rate of 5 °C min^{-1} under a static oxygen pressure of 2.5 Torr.

X-ray diffraction

A high-resolution X-ray diffractometer (Rigaku SmartLab) was used to perform θ–2θ line scans and X-ray reflectometry. A high-resolution X-ray diffractometer (Malvern Panalytical Empyrean) equipped with a 2D area detector was used to conduct 2D reciprocal space maps measurements. Synchrotron X-ray 3D reciprocal space mapping (3D-RSM) measurement was performed using a six-circle Huber diffractometer configured with Psi-C geometry at the beamline 7-ID-C of the APS at Argonne National Laboratory, utilizing X-rays with energies of 17.5 KeV (wavelength λ =

0.70846 Å). A Si (111) double-crystal monochromator with an energy resolution of ΔE/E = 1 × 10-4 was employed to fine-tune the X-ray energy. The X-ray beam at 7-ID-C, with a total flux of 3 × 10^12 photons per second at 17.5 keV, was optically focused by using Kirkpatrick-Baez (K-B) mirrors, resulting in a beam profile of 30 μm (Vertical) × 50 μm (Horizontal). Scattering signals were recorded using a Eiger2 X 500K 2D area detector, and the 2D images were subsequently processed. Geometric corrections were applied to all 3D-RSM data, which was further analyzed using the RSMap3D software developed at APS.

Scanning diffraction X-ray microscopy

Scanning diffraction X-ray microscopy (SDXM) measurement was performed at the Center for Nanoscale Materials' Hard X-ray Nanoprobe Beamline 26-ID at the upgraded Advanced Photon Source (APS) at Argonne National Laboratory. The X-ray beam energy was set to 10 keV, with a focused beam size of 40 nm full width at half-maximum (FWHM) achieved using a Fresnel zone plate. Diffraction patterns were collected by an Eiger2 X 1M detector positioned 1 meter from the sample, with a pixel size of 75 μm. SDXM tilt series were acquired at three sample angles, 18.3°, 18.5°, and 18.7°. Large field-of-view maps were obtained by stitching together eight SDXM maps, each covering an area of 6 × 6 um^2 with a step size of 60 nm.

Piezoresponse force microscopy

Dual AC Resonance Tracking (DART) piezoresponse force microscopy was conducted to image the domain structure with an MFP-3D Origin+ AFM (Asylum Research) using a conductive Pt/Ir coated conductive tip (Nanosensor, PPP-EFM, force constant ≈ 2.8 N m^{-1}).

Electrical measurements

Capacitor structures with symmetric $La_{0.7}Sr_{0.3}MnO_3$ electrodes were fabricated using photolithography followed by a wet etching process. After patterning the photoresist in circular shapes with diameters of 15, 25, 50, and 75 μm on the as-grown heterostructure, the sample was immersed in a diluted phosphoric acid solution (1 part acid: 5 parts deionized water) at 70 °C for 15 seconds to selectively etch away the $La_{0.7}Sr_{0.3}MnO_3$ top electrode regions that were not protected by the patterned photoresist. Eventually, the samples were immersed in acetone at 70 °C to remove the photoresist. Dielectric property measurements were conducted on at least 8 capacitors for each sample at room temperature. Dielectric permittivity and loss tangent were measured using an E4980A LCR meter (Agilent Technologies). PUND measurements were performed using a Precision Multiferroic Tester (Radiant Technologies). The capacitor structure was first pre-poled with a $-V_{Max}$ pulse to initialize its negative polarization state. The second pulse, $+V_{Max}$, switched the polarization, and the switched polarization (P*) was measured. Following this, the sample was allowed to settle at 0 V before a second measurement was taken to account for non-remanent polarization contributions. The third pulse ($+V_{Max}$) applied without switching, provided a measurement of the total non-remanent polarization (P^), followed by another 0 V measurement. The sequence was then mirrored for the negative voltage direction to complete the measurement. The P* represents switched polarization including both remanent and non-remanent polarization components. In contrast, the P^, measured during non-switching pulses, accounts only for the non-remanent contribution. Subtracting the P^ term from the P* term results in a measure of remanent-only polarization which is represented in (Fig. 4b and Supplementary Fig. 14). For this experiment, a pulse delay of 1 s and a pulse width of 0.01, 0.1, and 1 ms were used.

Microwave measurements were conducted on a gold interdigital capacitor (IDC) geometry fabricated using a lithographic process. A Keysight N5222B programmable network analyzer (PNA) was used to collect scattering parameters, while a Keithley 2612A source meter unit (SMU) supplied the bias voltage. The sample was probed using an MPI TS150 probe station equipped with FormFactor Infinity probes and SHF bias tees. Each two-port measurement began with a 0V bias applied to the probes. The bias voltage was then incrementally increased, alternating between positive and negative polarity. At each step, half of the total bias voltage was applied to each probe in opposite polarities. For instance, the first measurement applied 0 V to both probes, followed by +2.5 V and -2.5 V for a 5 V bias, then -2.5 V and +2.5 V for a -5 V bias, continuing this pattern until the maximum bias voltage was reached. A custom Python script automated data collection by controlling both the PNA and SMU. The acquired data included a complete set of two-port scattering parameters for each bias condition. A MATLAB script was used to compute key parameters such as capacitance and tunability from the acquired data.

Scanning transmission electron microscopy

The cross-sectional lamellae were prepared using a Thermo Fisher Helios G4 UX focused ion beam with the standard lift-out method. The HAADF-STEM images and 4D-STEM data for ptychographic reconstructions were acquired on a Thermo Fisher Spectra 300 X-CFEG STEM operated at 300 kV in nanoprobe mode with a semi-convergence angle of 30 mrad and probe current of 60 pA. The 4D-datasets for ptychography were collected on an EMPAD-G2 detector[62] operated at 2-10 kHz, with a probe overfocus of 10 nm and step-size of 0.42 Å. The ptychographic reconstructions used the least-squares maximum likelihood (LSQ-ML) multislice algorithm[63–65] in the fold-slice package[66,67] with 4 probe modes and slice thickness of 1-2 nm.

4D-STEM datasets for nanobeam diffraction were acquired on the EMPAD-G2 detector in microprobe mode with a semi-convergence angle of 1 mrad. We first performed cepstral transformation[68–70] on the 4D-data to reduce the impact of sample mistilts across the lamella. The phase-segmentation was done on the cepstral-transformed data through k-means clustering.

Second harmonic generation

Second harmonic generation (SHG) polarimetry was done with femtosecond pulses at λ = 800 nm fundamental light from a regeneratively amplified SpectraPhysics Ti:Sapphire laser system (1kHz, 80 fs). The schematic of the setup used for measurements is shown in Supplementary Figure 6. Linearly polarized light incident on the sample at 45^{o} generate second harmonic light at λ = 400 nm reflected off the sample. The *p*-polarized and *s*-polarized SHG intensities were spectrally filtered and measured by a photomultiplier tube through lock-in amplifier (SR830) detection. SHG Polar plots were generated by rotating the polarization angle (φ) of the incident fundamental light by a half-wave plate.

X-ray photoelectron spectroscopy

X-ray photoelectron spectroscopy (XPS) analyses were conducted using a PHI VersaProbe 4 equipped with a monochromatized Al Kα source. Spectra calibration was performed by aligning the adventitious carbon peak at 284.8 eV. The elemental stoichiometric ratios were quantified using the MultiPak software.

Density functional theory

Density functional theory (DFT) calculations were conducted on a (001)-oriented $NaNbO_3$ epitaxial film, using the generalized gradient approximation, within the Perdew-Burke-Ernzerhof functional for solids (PBEsol) as implemented in the Vienna Ab initio Simulation Package (VASP). The projector augmented wave approach is employed to treat the valence electrons, which account for 7 electrons for Na ($2p^6 3s^1$), 13 electrons for Nb ($4s^2 4p^6 4d^4 5s^1$), and 6 electrons for O ($2s^2 2p^4$). A plane-wave basis with a kinetic energy cutoff of 550 eV is used. The $NaNbO_3$ films are subject to a misfit strain η_{misfit}, ranging from $\simeq -4\%$ to $\simeq +4\%$, defined as $\eta_{misfit} = \frac{a-a_0}{a_0} \times 100\%$, where a represents the in-plane lattice constant of the substrate and a_0 is the in-plane lattice constant resulting from the energy minimization of the Cc phase.

To model perfect epitaxy on a cubic substrate, the strain tensor in Voigt notation has three elements that are frozen during each simulation: $\eta_1 = \eta_2 = \eta_{misfit}$ and $\eta_6 = 0$. Meanwhile, η_3, η_4, and η_5 are allowed to relax, along with all internal atomic coordinates, until the Hellmann-Feynman force on each atom is converged to below 0.001 eV/Å for each considered misfit strain. For the $NaNbO_3$ epitaxial film, the Cm symmetry used in the reference[47] was rotated clockwise by 90° to perform the DFT calculations.

Data availability

The datasets in the current study are available in the Dryad public repository at the following link: https://doi.org/10.5061/dryad.5dv41nsjf.

References

1. Jaffe, H. Piezoelectric ceramics. *J. Am. Ceram. Soc.* **41**, 494–498 (1958).
2. Noheda, B. & Cox, D. E. Bridging phases at the morphotropic boundaries of lead oxide solid solutions. *Phase Transitions* **79**, 5–20 (2006).
3. Izyumskaya, N. *et al.* Processing, Structure, Properties, and Applications of PZT Thin Films. *Crit. Rev. Solid State Mater. Sci.* **32**, 111–202 (2007).
4. Schönau, K. A. *et al.* Nanodomain structure of $Pb[Zr_{1-x}Ti_x]O_3$ at its morphotropic phase boundary: Investigations from local to average structure. *Phys. Rev. B* **75**, 184117 (2007).
5. Bellaiche, L., Garcia, A. & Vanderbilt, D. Finite-temperature properties of $Pb(Zr_{1-x}Ti_x)O_3$ alloys from first principles. *Phys. Rev. Lett.* **84**, 5427–5430 (2000).
6. Heitmann, A. A. & Rossetti, G. A., Jr. Thermodynamics of ferroelectric solid solutions with morphotropic phase boundaries. *J. Am. Ceram. Soc.* **97**, 1661–1685 (2014).
7. Wei, X.-K. *et al.* Ferroelectric phase-transition frustration near a tricritical composition point. *Nat. Commun.* **12**, 5322 (2021).
8. Bellaiche, L., García, A. & Vanderbilt, D. Electric-field induced polarization paths in $Pb(Zr_{1-x}Ti_x)O_3$ alloys. *Phys. Rev. B* **64**, (2001).
9. Cucchiella, F., D'Adamo, I., Lenny Koh, S. C. & Rosa, P. Recycling of WEEEs: An economic assessment of present and future e-waste streams. *Renewable Sustainable Energy Rev.* **51**, 263–272 (2015).
10. Koh, S. C. L. *et al.* Drivers of U.S. toxicological footprints trajectory 1998–2013. *Sci. Rep.* **6**, 39514 (2016).
11. Shrout, T. R. & Zhang, S. J. Lead-free piezoelectric ceramics: Alternatives for PZT? *J. Electroceram.* **19**, 111–124 (2007).

12. Waqar, M., Wu, H., Chen, J., Yao, K. & Wang, J. Evolution from lead-based to lead-free piezoelectrics: engineering of lattices, domains, boundaries, and defects Leading to giant response. *Adv. Mater.* **34**, e2106845 (2022).
13. Wang, X. *et al.* Giant piezoelectricity in potassium–sodium niobate lead-free ceramics. *J. Am. Chem. Soc.* **136**, 2905–2910 (2014).
14. Wu, J., Xiao, D. & Zhu, J. Potassium-sodium niobate lead-free piezoelectric materials: Past, present, and future of phase boundaries. *Chem. Rev.* **115**, 2559–2595 (2015).
15. Wu, B. *et al.* Giant piezoelectricity and high curie temperature in nanostructured alkali niobate lead-free piezoceramics through phase coexistence. *J. Am. Chem. Soc.* **138**, 15459–15464 (2016).
16. Zheng, T. *et al.* The structural origin of enhanced piezoelectric performance and stability in lead free ceramics. *Energy Environ. Sci.* **10**, 528–537 (2017).
17. Liu, Q. *et al.* High-performance lead-free piezoelectrics with local structural heterogeneity. *Energy Environ. Sci.* **11**, 3531–3539 (2018).
18. Tao, H. *et al.* Ultrahigh Performance in Lead-Free Piezoceramics Utilizing a Relaxor Slush Polar State with Multiphase Coexistence. *J. Am. Chem. Soc.* **141**, 13987–13994 (2019).
19. Zheng, T. *et al.* High-performance potassium sodium niobate piezoceramics for ultrasonic transducer. *Nano Energy* **70**, 104559 (2020).
20. Won, S. S. *et al.* Lead-free Mn-doped $(K_{0.5}Na_{0.5})NbO_3$ piezoelectric thin films for MEMS-based vibrational energy harvester applications. *Appl. Phys. Lett.* **108**, 232908 (2016).
21. Schlom, D. G., Chen, L. Q., Pan, X., Schmehl, A. & Zurbuchen, M. A. A thin film approach to engineering functionality into oxides. *J. Am. Ceram. Soc.* **91**, 2429–2454 (2008).
22. Dhole, S., Chen, A., Nie, W., Park, B. & Jia, Q. Strain engineering: A pathway for tunable

functionalities of perovskite metal oxide films. *Nanomaterials* **12**, 835 (2022).

23. Ahart, M. *et al.* Origin of morphotropic phase boundaries in ferroelectrics. *Nature* **451**, 545–548 (2008).

24. Zeches, R. J. *et al.* A strain-driven morphotropic phase boundary in BiFeO3. *Science* **326**, 977–980 (2009).

25. Zhang, J. X. *et al.* Large field-induced strains in a lead-free piezoelectric material. *Nat. Nanotechnol.* **6**, 98–102 (2011).

26. Christen, H. M., Nam, J. H., Kim, H. S., Hatt, A. J. & Spaldin, N. A. Stress-induced symmetry changes in $BiFeO_3$ films. *Phys. Rev. B* **83**, 144107 (2011).

27. Yang, J.-C., He, Q., Yu, P. & Chu, Y.-H. $BiFeO_3$ thin films: A playground for exploring electric-field control of multifunctionalities. *Annu. Rev. Mater. Res.* **45**, 249–275 (2015).

28. Xue, F., Li, Y., Gu, Y., Zhang, J. & Chen, L.-Q. Strain phase separation: Formation of ferroelastic domain structures. *Phys. Rev. B* **94**, 220101 (2016).

29. Everhardt, A. S. *et al.* Temperature-independent giant dielectric response in transitional $BaTiO_3$ thin films. *Appl. Phys. Rev.* **7**, 011402 (2020).

30. Peng, W. *et al.* Constructing polymorphic nanodomains in $BaTiO_3$ films via epitaxial symmetry engineering. *Adv. Funct. Mater.* **30**, 1910569 (2020).

31. Zhang, M.-H., Fulanovi, L., Zhao, C. & Koruza, J. Review on field-induced phase transitions in lead-free $NaNbO_3$-based antiferroelectric perovskite oxides for energy storage. *J. Materiomics* **9**, 1–18 (2023).

32. Zhang, M.-H. *et al.* Tailoring high-energy storage $NaNbO_3$-based materials from antiferroelectric to relaxor states. *Nat. Commun.* **14**, 1525 (2023).

33. Shimizu, H. *et al.* Lead-free antiferroelectric: $xCaZrO_3$-(1 - x)$NaNbO_3$ system ($0 \leq x \leq$

0.10). *Dalton Trans. J. Inorg. Chem.* **44**, 10763–10772 (2015).

34. Randall, C. A., Fan, Z., Reaney, I., Chen, L. Q. & Trolier-McKinstry, S. Antiferroelectrics: History, fundamentals, crystal chemistry, crystal structures, size effects, and applications. *J. Am. Ceram. Soc.* **104**, 3775–3810 (2021).

35. Liu, Z. *et al.* Antiferroelectrics for energy storage applications: a review. *Adv. Mater. Technol.* **3**, 1800111 (2018).

36. Wang, G. *et al.* Electroceramics for high-energy density capacitors: current status and future perspectives. *Chem. Rev.* **121**, 6124–6172 (2021).

37. Schwarzkopf, J. *et al.* Strain-induced phase transitions in epitaxial $NaNbO_3$ thin films grown by metal-organic chemical vapour deposition. *J. Appl. Crystallogr.* **45**, 1015–1023 (2012).

38. Duk, A., Schmidbauer, M. & Schwarzkopf, J. Anisotropic one-dimensional domain pattern in $NaNbO_3$ epitaxial thin films grown on (110) $TbScO_3$. *Appl. Phys. Lett.* **102**, 2011–2015 (2013).

39. Sellmann, J. *et al.* Strained ferroelectric $NaNbO_3$ thin films: Impact of pulsed laser deposition growth conditions on structural properties. *Thin Solid Films* **570**, 107–113 (2014).

40. Wu, H. *et al.* Alkali-deficiency driven charged out-of-phase boundaries for giant electromechanical response. *Nat. Commun.* **12**, 2841 (2021).

41. Patel, K., Prosandeev, S., Xu, B., Xu, C. & Bellaiche, L. Properties of (001) $NaNbO_3$ films under epitaxial strain: A first-principles study. *Phys. Rev. B.* **103**, 094103 (2021).

42. de Oliveira Guimarães, M. *et al.* Ferroelectric phase transitions in tensile-strained $NaNbO_3$ epitaxial films probed by in situ x-ray diffraction. *J. Appl. Phys.* **132**, 154102 (2022).

599 43. Bin Anooz, S. *et al.* High temperature phase transitions in $NaNbO_3$ epitaxial films grown
600 under tensile lattice strain. *Appl. Phys. Lett.* **120**, 202901 (2022).
601 44. Schneider, T., Cardoletti, J., Komissinskiy, P. & Alff, L. Impact of strain engineering on
602 antiferroelectricity in $NaNbO_3$ thin films. *ACS Omega* **8**, 23587–23595 (2023).
603 45. Liu, H. *et al.* Giant piezoelectricity in oxide thin films with nanopillar structure. *Science*
604 **369**, 292–297 (2020).
605 46. Lin, B. *et al.* Ultrahigh electromechanical response from competing ferroic orders. *Nature*
606 **633**, 798–803 (2024).
607 47. Harikrishnan, K. *et al.* Electron ptychography reveals a ferroelectricity dominated by anion
608 displacements. *arXiv:2408.14795 [cond-mat.mtrl-sci]* (2024).
609 48. Glazer, A. M. & Megaw, H. D. Studies of the lattice parameters and domains in the phase
610 transitions of $NaNbO_3$. *Acta Crystallogr. A* **29**, 489–495 (1973).
611 49. Vanderbilt, D. & Cohen, M. H. Monoclinic and triclinic phases in higher-order Devonshire
612 theory. *Phys. Rev. B Condens. Matter* **63**, 094108 (2001).
613 50. Damodaran, A. R. *et al.* Nanoscale structure and mechanism for enhanced
614 electromechanical response of highly Strained $BiFeO_3$ thin films. *Adv. Mater.* **23**, 3170–
615 3175 (2011).
616 51. Chen, Z. *et al.* Low-symmetry monoclinic phases and polarization rotation path mediated
617 by epitaxial strain in multiferroic $BiFeO_3$ thin films. *Adv. Funct. Mater.* **21**, 133–138
618 (2011).
619 52. Chen, Z. *et al.* Coexistence of ferroelectric triclinic phases in highly strained $BiFeO_3$ films.
620 *Phys. Rev. B* **84**, 1–6 (2011).
621 53. Schneider, T. *et al.* Evidence for antipolar displacements in $NaNbO_3$ thin films. *Appl. Phys.*

Lett. **121**, 122906 (2022).

54. Mino, T. *et al.* Piezoelectric properties of epitaxial $NaNbO_3$ Thin films deposited on (001)SrRuO3/pt/MgO substrates. *Jpn. J. Appl. Phys.* **46**, 6960–6963 (2007).

55. Yamazoe, S., Sakurai, H., Fukada, M., Adachi, H. & Wada, T. The effect of $SrTiO_3$ substrate orientation on the surface morphology and ferroelectric properties of pulsed laser deposited $NaNbO_3$ films. *Appl. Phys. Lett.* **95**, 062906 (2009).

56. Saito, T., Adachi, H., Wada, T. & Adachi, H. Pulsed-laser deposition of ferroelectric $NaNbO_3$ thin films. *Jpn. J. Appl. Phys. (2008)* **44**, 6969 (2005).

57. Bassiri-Gharb, N. *et al.* Domain wall contributions to the properties of piezoelectric thin films. *J. Electroceram.* **19**, 47–65 (2007).

58. Agar, J. C. *et al.* Tuning susceptibility via misfit strain in relaxed morphotropic phase boundary $PbZr_{1-x}Ti_xO_3$ epitaxial thin films. *Adv. Mater. Interfaces* **1**, 1400098 (2014).

59. Oikawa, T., Aratani, M., Funakubo, H., Saito, K. & Mizuhira, M. Composition and orientation dependence of electrical properties of epitaxial $Pb(Zr_xTi_{1-x})O_3$ thin films grown using metalorganic chemical vapor deposition. *J. Appl. Phys.* **95**, 3111–3115 (2004).

60. Berlincourt, D., Cmolik, C. & Jaffe, H. Piezoelectric properties of polycrystalline lead titanate zirconate compositions. *Proc. IRE* **48**, 220–229 (1960).

61. Bastani, Y. & Bassiri-Gharb, N. Enhanced dielectric and piezoelectric response in PZT superlattice-like films by leveraging spontaneous Zr/Ti gradient formation. *Acta Mater.* **60**, 1346–1352 (2012).

62. Philipp, H. T. *et al.* Very-high dynamic range, 10,000 frames/second pixel array detector for electron microscopy. *Microsc. Microanal.* **28**, 1–16 (2022).

63. Thibault, P. & Guizar-Sicairos, M. Maximum-likelihood refinement for coherent diffractive

imaging. *New J. Phys.* **14**, 063004 (2012).

64. Tsai, E. H. X-ray ptychography with extended depth of field. *Optics Express* **24**, 29089–29108 (2016).

65. Maiden, A. M., Humphry, M. J. & Rodenburg, J. M. Ptychographic transmission microscopy in three dimensions using a multi-slice approach. *J. Opt. Soc. Am. A Opt. Image Sci. Vis.* **29**, 1606–1614 (2012).

66. Wakonig, K. *et al.* PtychoShelves, a versatile high-level framework for high-performance analysis of ptychographic data. *J. Appl. Crystallogr.* **53**, 574–586 (2020).

67. Chen, Z. *et al.* Electron ptychography achieves atomic-resolution limits set by lattice vibrations. *Science* **372**, 826–831 (2021).

68. Padgett, E. *et al.* The exit-wave power-cepstrum transform for scanning nanobeam electron diffraction: robust strain mapping at subnanometer resolution and subpicometer precision. *Ultramicroscopy* **214**, 112994 (2020).

69. Harikrishnan, K. P. *et al.* Dose-efficient strain mapping with high precision and throughput using cepstral transforms on 4D-STEM data. *Microsc. Microanal.* **27**, 1994–1996 (2021).

70. Yoon, D., Kp, H., Shao, Y.-T. & Muller, D. A. High-speed, high-precision, and high-throughput strain mapping with cepstral transformed 4D-STEM data. *Microscopy and Microanalysis* **28**, 796–798 (2022).

Acknowledgments

R.G. and R.X. acknowledge the support from the National Science Foundation (NSF) under award No. DMR-2442399 and the American Chemical Society Petroleum Research Fund under award No. 68244-DNI10. K.P., S.P. and L.B. thank an ARA Impact Grant 3.0, the Vannevar Bush

669 Faculty Fellowship (VBFF) Grant No. N00014-20-1-2834 from the Department of Defense. K.P.,
670 S.P., L.B., H.K., and D.A.M. acknowledge funding from the ETHOS MURI grant W911NF-21-2-
671 0162 from the Army Research Office (ARO). A.K., K.J.C., and H.Y.H. acknowledge support by
672 the U.S. DOE, Office of Basic Energy Sciences, Division of Materials Sciences and Engineering
673 under Contract No. DE-AC02-76SF00515. S.H. and V.G. acknowledge support from the DOE-
674 BES under grant number DE-SC0012375 for optical second harmonic generation measurements.
675 D.S acknowledges support from the NSF under award number DMR-2143642 for sample
676 fabrication. L.W., C.J.G.M., and J.E.S. acknowledge support from the U.S. Army Research
677 Laboratory under Cooperative Agreement No. W911NF-24-2-0100, and J.E.S. acknowledges
678 support also from the U.S. Army Research Office under grant W911NF-21-1-0126. M.C.
679 acknowledges support from the U.S. Department of Energy, Office of Basic Energy Sciences,
680 Division of Materials Sciences and Engineering under contract FWP-ERKCS89. Y.K. is supported
681 by BES-ECA ERKCZ55. Part of the microscopy work was performed at the Center for Nanophase
682 Materials Sciences (CNMS), a DOE Office of Science User Facility at ORNL. This work was
683 supported by the NSF, as part of the Center for Dielectrics and Piezoelectrics under grant nos. IIP-
684 1841453 and IIP-1841466. Work performed at the Center for Nanoscale Materials and Advanced
685 Photon Source, both U.S. Department of Energy Office of Science User Facilities, was supported
686 by the U.S. DOE, Office of Basic Energy Sciences, under Contract No. DE-AC02-06CH11357.
687 The electron microscopy studies made use of the Cornell Center for Materials Research shared
688 instrumentation facility instruments supported by the NSF (DMR-2039380). Part of this work was
689 performed at the Stanford Nano Shared Facilities (SNSF) RRID:SCR_023230, supported by the
690 National Science Foundation under award ECCS-2026822. This work was performed in part at the
691 Analytical Instrumentation Facility (AIF) at North Carolina State University, which is supported

692 by the State of North Carolina and the National Science Foundation (award number ECCS-
693 2025064). The AIF is a member of the North Carolina Research Triangle Nanotechnology
694 Network (RTNN), a site in the National Nanotechnology Coordinated Infrastructure (NNCI).

Author contributions

R.X. conceived and supervised the study. R.X. and R.G. designed the experiments. R.G. synthesized the thin film samples and performed PFM characterizations and analysis, with contributions from H.Q. and N.B. R.G. also carried out capacitor fabrication and electrical measurements, with support from Y.N. and D.S. H.K. and D.A.M. conducted electron ptychography and analysis. K.P., S.P., and L.B. performed the DFT simulations. R.G., A.K., and K.J.C. conducted lab-source X-ray diffraction measurements, with support from H.Y.H. H.Z. performed synchrotron X-ray reciprocal space mapping. T.Z., R.L., and M.H. carried out synchrotron X-ray scanning diffraction microscopy, with contributions from Y.K. and M.C. J.W. conducted XPS measurements and analysis. L.W., J.C., C.J.G.M., and J.E.S. conducted microwave measurements. S.H. and V.G. performed SHG measurements and analysis. R.X. and R.G. wrote the manuscript with input from all authors.

Competing interests

The authors declare no competing interests.

Main Figures

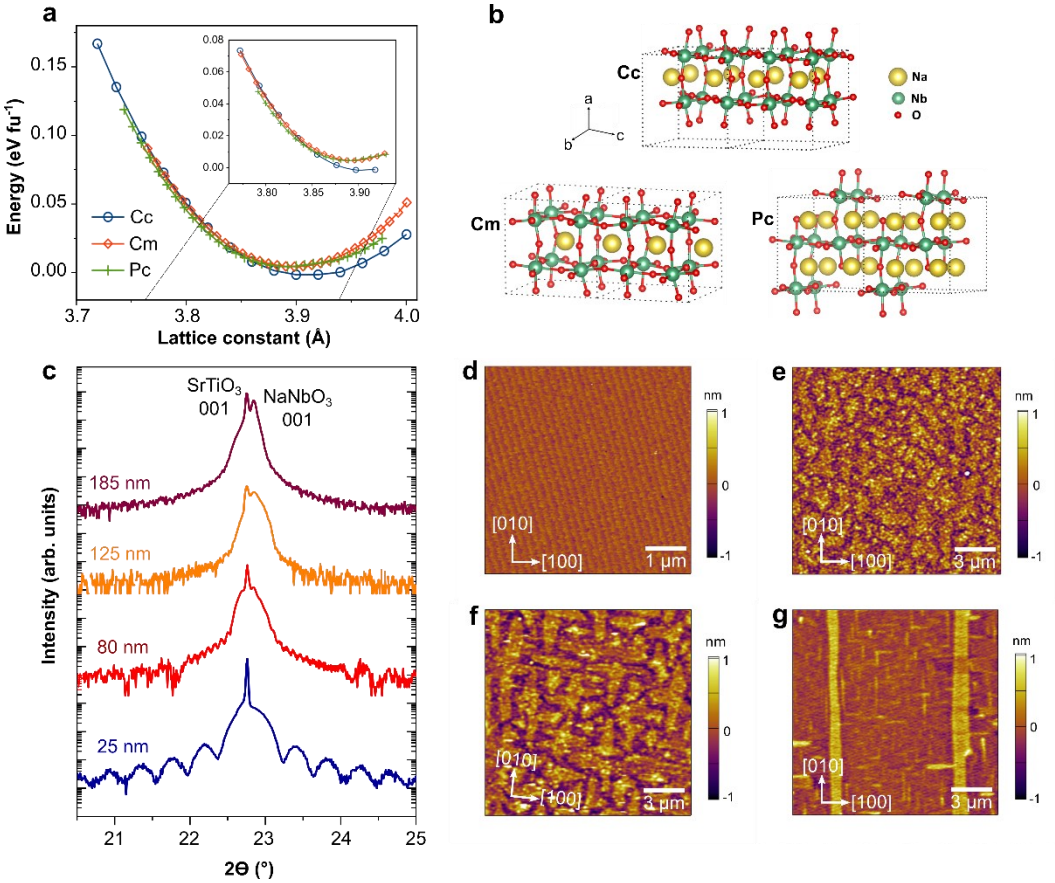

Figure 1 | Structural phase and topography evolution of $NaNbO_3/SrTiO_3$ (001) heterostructures with varying film thickness. (a) Total energy as a function of lattice parameter for the *Cc*, *Cm*, and *Pc* phases in (001)-oriented epitaxial $NaNbO_3$ thin films. The inset provides a magnified view of the energy curve in the range of 3.76–3.94 Å. **(b)** Schematic representations of the atomic structures of the *Cc*, *Cm*, and *Pc* phases in (001)-oriented epitaxial $NaNbO_3$ thin films. **(c)** X-ray θ-2θ diffraction patterns of $NaNbO_3/SrTiO_3$ (001) heterostructures as a function of film thickness, measured near the pseudocubic (001) diffraction condition. **(d–g)** Atomic force microscopy (AFM) images of $NaNbO_3$ films with thicknesses of **(d)** 25 nm, **(e)** 80 nm, **(f)** 125 nm, and **(g)** 185 nm. The 25 nm films exhibit atomically smooth surfaces, while labyrinthine topographical patterns emerge with increasing film thickness.

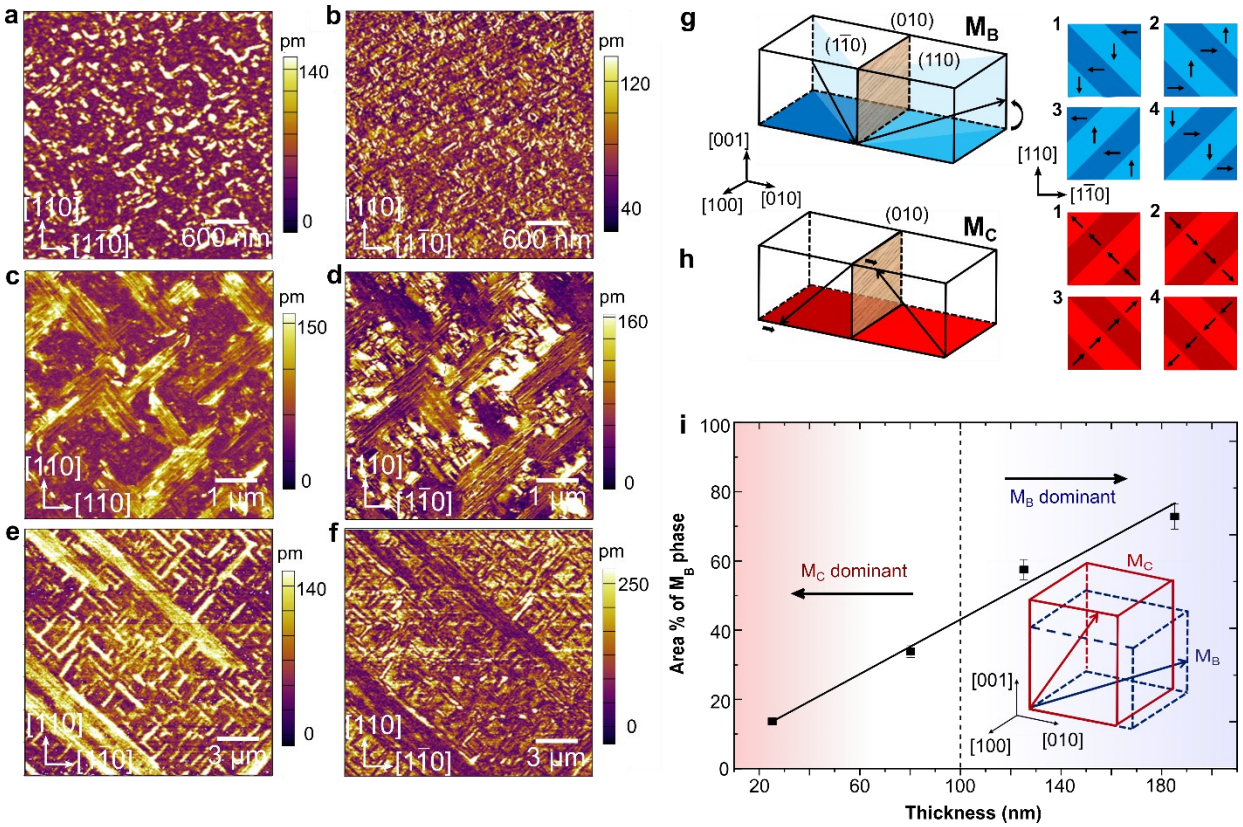

Figure 2 | Ferroelectric domain structure evolution of $NaNbO_3/SrTiO_3$ (001) heterostructures with varying film thickness. **(a, c, e)** Vertical and **(b, d, f)** lateral piezoresponse force microscopy (PFM) amplitude imaging, along with corresponding schematic representations of the M_C (red) and M_B (blue) phases for $NaNbO_3$ films with thicknesses of **(a, b)** 25 nm, **(c, d)** 80 nm, and **(e, f)** 185 nm, respectively. Schematic representations of the polarization configurations with charge neutral domain walls for **g)** M_B and **h)** M_C phases, respectively, with corresponding in-plane projection schematics for the possible polydomain configurations. **(i)** Areal fraction of the M_B phase as a function of thickness, showing an increase in M_B phase and a decrease in M_c phase with increasing film thickness.

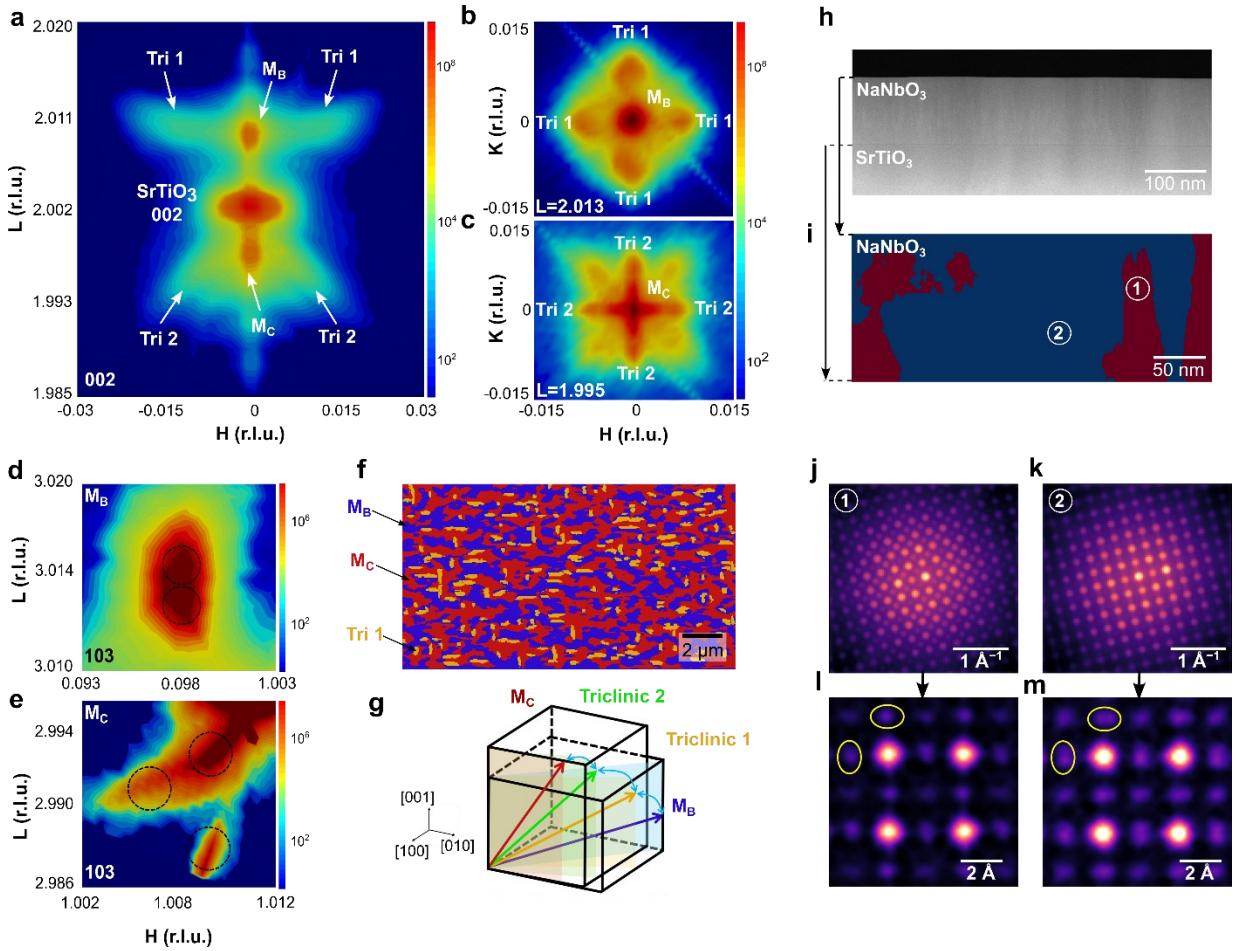

Figure 3 | Elucidating the microstructure of mixed phases in $NaNbO_3/SrTiO_3$ heterostructures. Synchrotron X-ray reciprocal space map (RSM) near the 002-diffraction condition for an 80 nm $NaNbO_3/SrTiO_3$ heterostructure, revealing two distinct peaks corresponding to the M_B and M_C phases, along with surrounding satellite peaks from the triclinic phase in the **(a)** HL-plane, **(b)** HK-plane at L = 2.013, and **(c)** HK-plane at L = 1.995. Zoomed-in RSMs near the 103-diffraction condition for the **(d)** M_B and **(e)** M_C phases of an 80 nm $NaNbO_3$ film show peak splitting, as highlighted in Supplementary Fig. 10. **(f)** Scanning diffraction X-ray microscopy (SDXM) dark-field imaging depicts the coexistence of M_B (blue), M_C (red), and bridging Triclinic 1 (Tri-1, orange) phases. **(g)** Schematic illustration of the polarization rotation pathway between the M_C and M_B phases, facilitated by intermediate triclinic phases. **(h)** HAADF-STEM image of the $NaNbO_3/SrTiO_3$ heterostructure. **(i)** Nanoscale spatial distribution of two distinct phases in the $NaNbO_3$ film, identified in red and blue via segmentation of nanobeam electron diffraction data. **(j, k)** Average diffraction patterns from the two segmented regions, showing the presence **(j)** or absence **(k)** of half-order diffraction spots indicative of in-phase and anti-phase octahedral tilts, respectively. **(l, m)** Ptychographic images of a 2 × 2 pseudo-cubic unit-cell region of the two phases, illustrating **(l)** in-phase and **(m)** anti-phase octahedral tilting. These tilt modes are distinguished by singular or split oxygen sites, highlighted with yellow ovals.

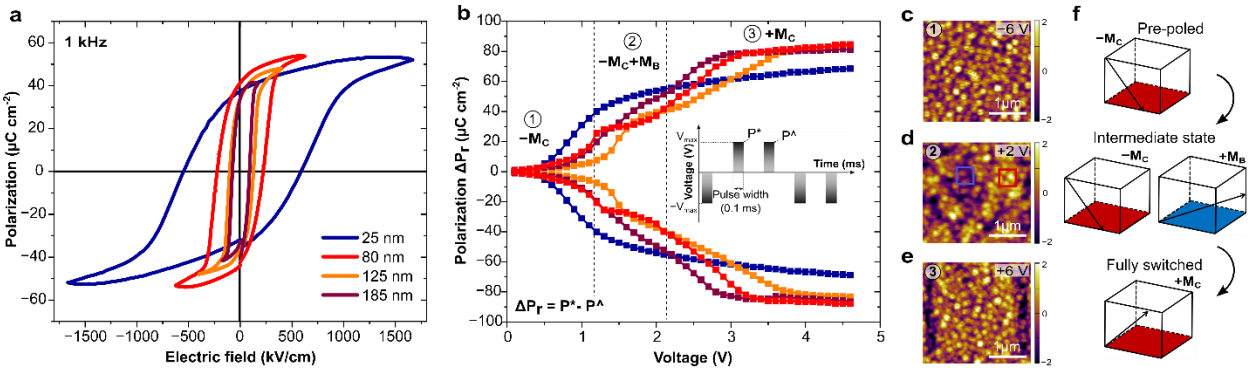

Figure 4 | Ferroelectric switching properties of $NaNbO_3$ films with varying thickness. (a) Polarization-electric field (*P*-*E*) hysteresis loops as a function of film thickness, measured at 1 kHz. **(b)** Thickness-dependent positive-up, negative down (PUND) measurements of $NaNbO_3$ films with varying thickness. The switched remanent polarization (ΔP_r) is measured as a function of applied voltage at a pulse width of 0.1 ms and a pulse delay of 1s. The pulse switching results indicate a multi-state switching pathway, with the presence of an intermediate polarization state, arising from a mixture of negatively poled M_C and positively poled M_B phases. **(c-e)** AFM topography evolution of 80 nm-thick $NaNbO_3$ film after poling at **(c)** -6 V, **(d)** 2 V, and **(e)** 6 V, revealing the emergence of a labyrinthine pattern upon the intermediate poling voltage. **(f)** Corresponding schematic representations illustrate the field-driven phase evolution in $NaNbO_3$ films: the negatively poled M_C phase initially transitions into an intermediate state, where the negatively poled M_C and positively poled M_B phases coexist under the reversal field, before fully switching into a positively poled M_C phase.

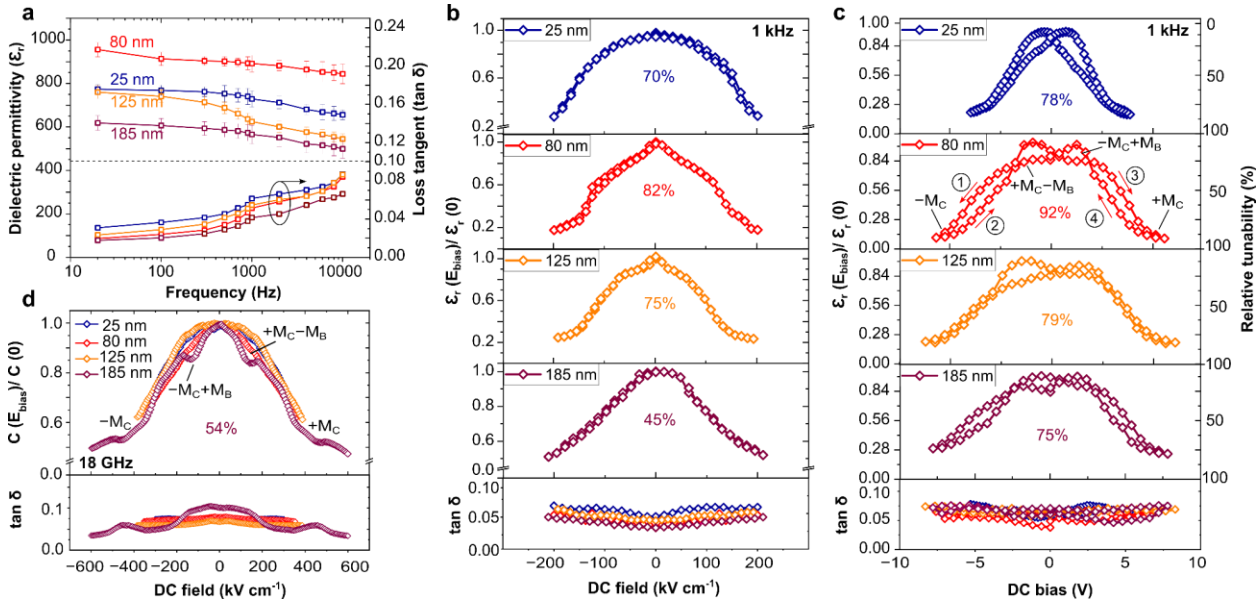

Figure 5 | Thickness-dependent dielectric property evolution of $NaNbO_3$ thin films. (a) Dielectric permittivity and loss tangent measured as a function of frequency (20 Hz–10 kHz) at an AC excitation voltage of 5 mV for $NaNbO_3$ films with varying thickness. Normalized dielectric permittivity as a function of DC field **(b)** up to 220 kV/cm (below the coercive field), and as a function of DC bias **(c)** up to 8 V (above the coercive field), with tunability ($\Delta\varepsilon_r(\text{bias})/\varepsilon_r(0)$) extracted for each thickness. Measurements in **(b)** and **(c)** were performed on vertical capacitor structures with symmetric $La_{0.7}Sr_{0.3}MnO_3$ electrodes at 1 kHz. The unconventional tunability behavior shown in **(c)** is attributed to the multi-state switching pathway in mixed-phase $NaNbO_3$, where an intermediate mixed phase state (i.e., coexistence of negatively poled M_B and positively poled M_C or vice versa) maintains minimal permittivity change under a DC field. The direction of DC bias application is indicated for the 80 nm-thick film. **(d)** Normalized capacitance and loss tangent measured at 18 GHz using an in-plane interdigital capacitor geometry on $NaNbO_3/SrTiO_3$ heterostructures with varying film thickness. A maximum tunability of 54% was observed in 185 nm films, exhibiting unconventional tunability behavior due to the presence of an intermediate polarization state.